INTERFACE FOCUS

royalsocietypublishing.org/journal/rsfs

Research

Cite this article: Gauci F-X, Jami L, Keiser L, Cohen C, Noblin X. 2025 Channel deformations during elastocapillary spreading of gaseous embolisms in biomimetic leaves. *Interface Focus* **15**: 20240060.
https://doi.org/10.1098/rsfs.2024.0060

Received: 23 December 2024
Accepted: 1 April 2025

One contribution of 8 to a theme issue 'Capillarity and Elastocapillarity in Biology'.

Subject Areas:
biomimetics, biophysics

Keywords:
leaves, microfluidics, embolism, bubbles, elastocapillarity

Author for correspondence:
Xavier Noblin
e-mail: xavier.noblin@univ-cotedazur.fr

THE ROYAL SOCIETY PUBLISHING

Channel deformations during elastocapillary spreading of gaseous embolisms in biomimetic leaves

François-Xavier Gauci, Ludovic Jami, Ludovic Keiser, Céline Cohen and Xavier Noblin

CNRS UMR 7010, Institut de Physique de Nice, Université Côte d'Azur, Nice, Provence-Alpes-Côte d'Azur, France

F-XG, 0009-0000-1896-3874; LJ, 0000-0002-8822-7669; LK, 0000-0002-1681-9606; XN, 0000-0002-1787-4682

The nucleation and/or spreading of bubbles in water under tension (due to water evaporation) can be problematic for most plants along the ascending sap network—from roots to leaves—called xylem. Due to global warming, trees facing drought conditions are particularly threatened by the formation of such embolisms, which hinders sap flow and can ultimately be fatal. Polydimethylsiloxane (PDMS)-based biomimetic leaves simulating evapotranspiration have demonstrated that, in a linear configuration, the existence of a slender constriction in the channel allows for the creation of intermittent embolism propagation (as an interaction between the elasticity of the biomimetic leaf and the capillary forces at the air/water interfaces) (Keiser *et al*. 2022 *J. Fluid Mech.* **948**, A52 (doi:10.1017/jfm.2022.733); Keiser *et al*. 2024 *J. R. Soc. Interface* **21**, 20240103 (doi:10.1098/rsif.2024.0103)). Here, we use analogue PDMS-based biomimetic leaves in one dimension and two dimensions. To better explore the embolism spreading mechanism, we add to the setup an additional technique, allowing to measure directly the microchannel's ceiling deformation versus time, which corresponds to the pressure variations. We present here such a method that allows one to have quantitative insights into the dynamics of embolism spreading. The coupling between channel deformations and the Laplace pressure threshold explains the observed elastocapillary dynamics.

1. Introduction

The nucleation and growth of bubbles in plants can have dramatic (positive or negative) impacts. In the process of fern spores' ejection, the nucleation of cavitation bubbles in water under tension triggers the fast catapulting mechanism. The origin of this fast motion lies in the deformation of a catapult-like elastic structure (the annulus) induced by water evaporation. This later leads to the annulus compartment volume decreasing and negative pressure building up, up to the nucleation of a cavitation bubble. This later triggers the fast catapulting mechanism that we have studied in biological and artificial systems [1,2]. The same phenomenon of sudden spreading of gas bubbles in water under tension (due to water evaporation) can be problematic for most plants. In plants, the sap circulates from roots to leaves through the veins of their xylem system. A vein consists in a bundle made of sequences of hollow tracheary elements. Theoretical explanation for sap flows in trees was described in 1895 by the cohesion-tension theory [3]. The driving force behind the rise of sap in plants is the evaporation occurring in leaves. It creates a gradient of pressure along the water-filled xylem that pulls the water column upwards [4–6]. It allows the sap to rise several tens of metres from roots to leaves but in return, leads to a risk of emergence of gas embolism, namely, the spreading of gas inside the hydraulic network, which can inhibit or even block the sap circulation and seriously impact the productivity of the plants [7]. This risk of embolism

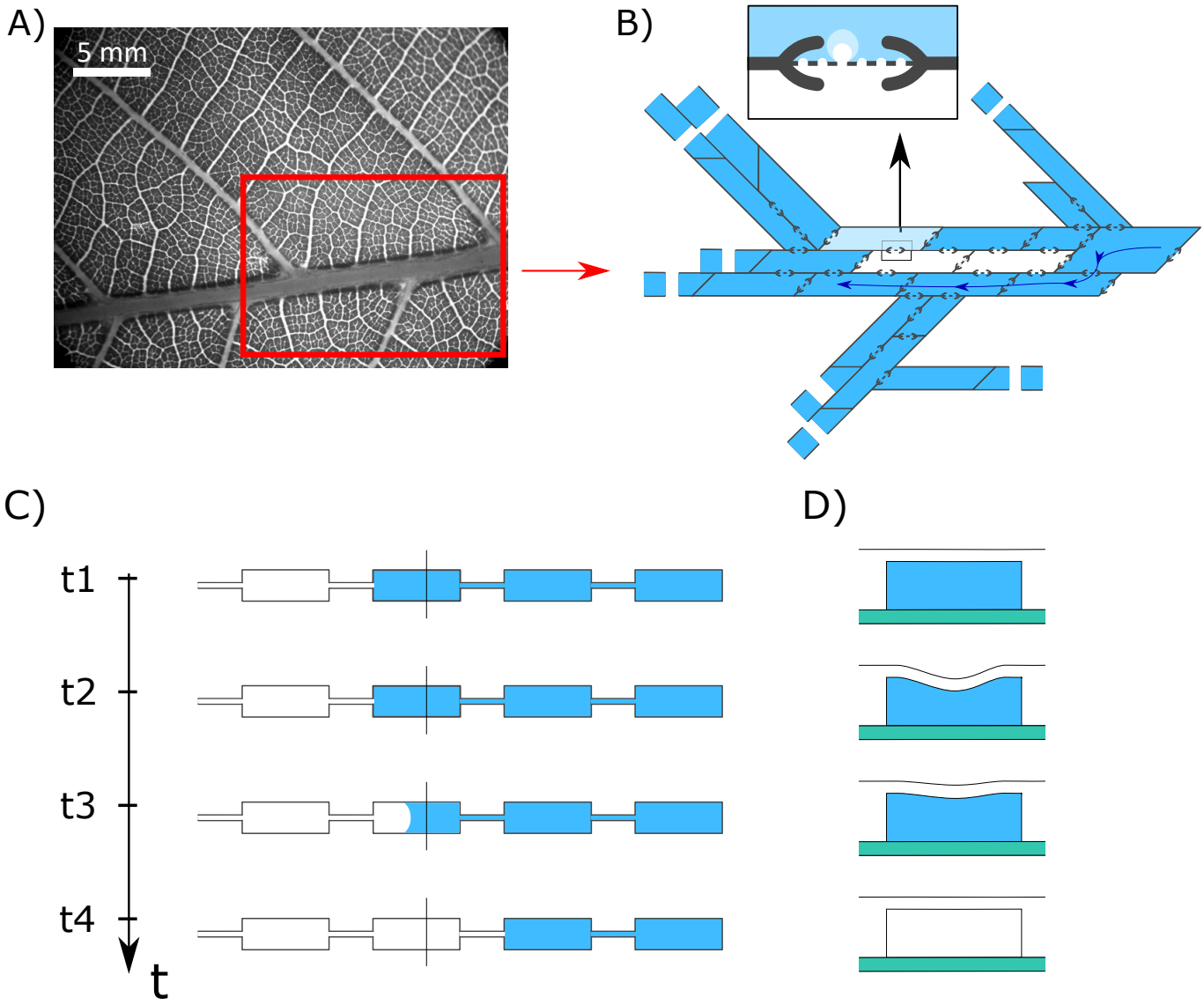

Figure 1. (A) Image of a leaf of walnut tree (acknowledgement to Virgile Thiévenaz). (B) Schematic of xylem tracheary elements connected by bordered pits with embolism spreading. This schematic is a highly simplified depiction of the complex and not fully understood processes that occur under the extreme thermodynamic conditions in xylem. In particular, it does not incorporate mechanisms such as the potential formation of nanobubbles [10,17] or the limiting role of air diffusion in embolism propagation [18]. (C) Top view of a one-dimensional biomimetic system with identical channels connected by narrower constrictions at various times during embolism propagation. Although these PDMS constrictions capture the essential capillary 'valve' function of bordered pits, they necessarily omit the intricate nanofibrous architecture and multiscale complexity of real pit membranes [19,20]. Nonetheless, this design is sufficient for our present focus on embolism dynamics in a controlled environment. (D) Side views (taken at black lines locations) of the deformation of the microchannel ceilings as the embolism passes through it, due to the capillary pressure imposed at the embolism/liquid interface.

formation is dramatically increased by conditions of water stresses in soils, as well as in situations of vapour pressure deficit [8]. Global warming and its consequences in terms of increase of drought event frequency and intensity will put most forests across the globe in danger of survival [9].

Mechanisms at the origin of gas embolism in xylem are still not clearly established and could be various. A tension too high can generate cavitation events [10,11] or it may come from pre-existing gas bubbles [12] or air-seeding, originating from outside.

In leaves, embolisms can be observed spreading intermittently and result in catastrophic events [13]. Polydimethylsiloxane (PDMS) based biomimetic leaves simulating evapotranspiration have demonstrated that, in a one-dimensional configuration, the presence of a slender constriction in the channel allows for the creation of intermittent embolism propagation. This results from an interaction between the elasticity of the biomimetic leaf (mainly the deformable channel ceiling) and the capillary forces at the air/water interfaces [14,15].

Once inside the system, embolism spreads step by step in the xylem, intermittently and hierarchically [13,16]. On the one hand, the intermittency is characterized by fast events of embolism propagation in veins, followed by pauses. This comes from the presence of bordered pits longitudinally and laterally connecting tracheary elements (figure 1B) [21]. These micrometric holes contain cellulosic mesh and act as defence valves that momentarily contain the embolism. On the other hand, hierarchical spreading manifests itself by starting preferentially from the main veins (the midrib and secondary veins) and ending by the thinnest ones (higher-order veins).

The three-dimensional structure of a leaf, its variety of materials, size scales and its complex structure make it difficult to interpret a transmission view of a drying leaf. A biomimetic approach makes images acquisition simpler, allows one to control parameters and environmental conditions more accurately and isolates specific physical ingredients.

Leaves evapotranspiration can be reproduced, using PDMS owing to its permeability to gas and water [22], so a microchannel network can be built to create a drying PDMS leaf venation system.

The presence of pits has already been mimicked artificially by linking two PDMS microchannels with a narrower one [14], though this remains an oversimplification compared to natural bordered pits (figure 1B), which possess a bordering part and a highly multiscale nanoporous structure rather than a single micro-scale constriction (figure 1C). When the air/water interface gets into the constriction, its curvature increases strongly, lowering pressure in the exit liquid-filled channel. As the interface crosses the constriction and its curvature decreases, the water pressure rises again—a phenomenon analogous to the well-documented Haines jump in porous media [23], and one that is also presumed to occur in plant xylem and to exhibit acoustic emissions [24,25]. The nonlinear dynamics of the meniscus comes from an elastocapillary coupling between the compliance of the channel and the interface curvature, forced to sustain large changes to get through the constriction. Experiments with several identical channels in series have also been performed [15] in which a sequence of jumps and stops of the meniscus is observed, due to the presence of constrictions. As discussed in previous work [15], there remain significant gaps between these artificial PDMS replicas and plant leaves. In natural xylem, the porous, fibrous architecture of pit membranes, surface-active solutes in the sap, and complex mechanical properties of lignified cell walls can drastically affect embolism formation and propagation [10,12,26]. Additionally, plant leaves often operate under negative pressures and involve symplastic/apoplastic water transport pathways, aspects that our current macroscale PDMS channels do not replicate [27,28]. While these biomimetic devices capture some key physical ingredients—namely, the interplay of elasticity, capillarity and evaporative drying—they remain strong simplifications relative to *in vivo* systems. A additional simplification lies in the geometry of the microchannels which are of square or rectangular section compare to the cylindrical one in real plants. Although the shape/geometry may be important, the main features that have to be taken under consideration, as shown up to now, are really more related to size than geometry (for example for the critical pressure). From a microfluidics point of view, the flow properties of a square or rectangular channel section compared to a cylinder are not so different (except a numerical coefficient for the pressure-flow rate law).

Acknowledging such drawbacks, we aim here to further bridge the gap between bio-inspired microfluidic experiments and actual leaves. Building upon the state-of-the-art design in [14,15,29], we introduce in the present study (i) direct pressure measurements *in situ* via an interferometric technique and (ii) a two-dimensional reticulate network, to more closely reflect the branching geometry of biological venation systems. Through this combined approach, we hope to gain additional insight into the elastocapillary dynamics underlying embolism propagation in water-stressed channels, while keeping in mind the ultimate goal of transferring such knowledge to plant systems.

In this article, we first present the materials and methods (§2), with the biomimetic devices used (§2.1), along with the interferometric deformation measurement method developed and its calibration of the device to measure pressure variations (§2.2). We then present results obtained for the pressure variations versus time in both the one-dimensional and two-dimensional systems (§3). We then discuss these findings together with perspectives for future developments (§4).

2. Material and methods

2.1. The biomimetic pervaporation leaf setup

2.1.1. Biomimetic leaf

We used two types of devices: (i) in one dimension, the same as used in [15] where identical channels elements are connected by identical constriction much narrower than the channels. The height and the width of the constrictions are, respectively, 48 µm and 22 µm while the channels have the same depth but a width of 303 µm (figure 1C).

(ii) In two dimensions, we used a new device composed of interconnected microchannels presenting between one and four neighbours of different widths connected by a constriction of height 38 µm and width 20 µm. The schematic is presented in figure 5A.

The PDMS devices have been made following a classical protocol of soft lithography [30]. To do so, we first designed the photolithography masks using a Python program which returns a svg file that has been printed on a plastic film by the Selba company. Then, we created the network mould in SU8 negative resist (MicroChem) from which we made the final PDMS device. To ensure a reduced thickness of the ceiling above the channels, the mixture of liquid PDMS (SylgardTM 184, from Dow) and curing agent (in the mass fraction 10:1) is spin-coated over the SU8 mould. The liquid PDMS mixture in the mould is then degassed under vacuum and heated in a oven at 65°C during 24 h to obtain a thin sheet of PDMS that we hereafter call PDMS membrane.

Once the PDMS membrane is reticulated, it is removed from the mould and put on a plasma-treated glass slide. With a scalpel, we perform a wide cut at the 'petiole' end (which is the base of a leaf network connected to the rest of the tree; for us, it is the entry point for the air in our device), creating a direct connection between the network entrance and the outside. The system is then immersed in water in an open Petri dish and placed under vacuum inside a desiccator during several hours. The air leaves the microchannels, which fill with water coming from the cut. We obtained the biomimetic leaf which will be used for the embolism experiment.

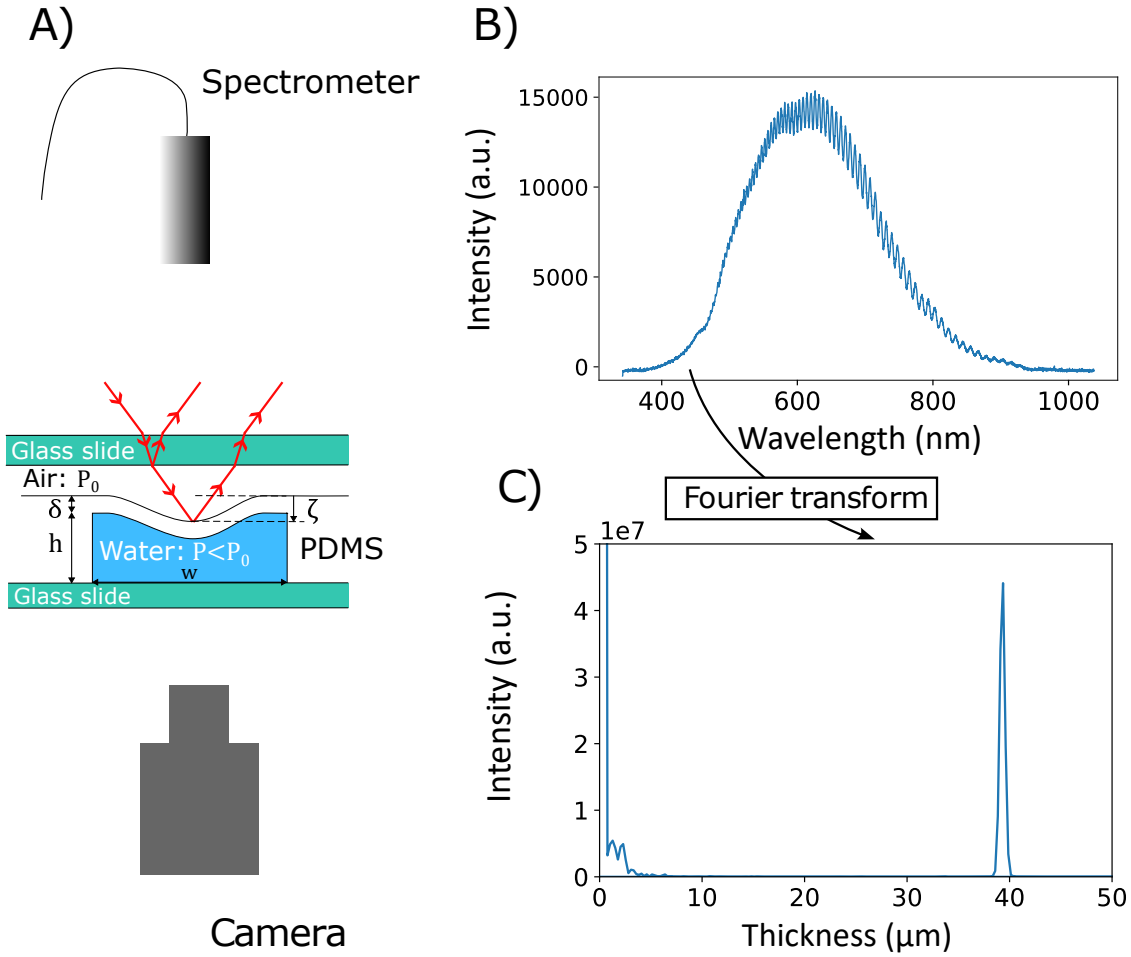

Figure 2. (A) Setup with camera and spectrometer to record the spectra for thickness measurements. (B) Spectrum showing oscillations due to the air thickness between the glass slide and the ceiling of the microchannel. (C) Fourier transform of the spectrum, giving a peak at the thickness measured, enabling one to deduce the pressure inside the microchannel.

2.1.2. Pervaporation setup

The imaging setup is composed as follows. A uniform white light source (MetaBright Backlight MB-BL410) is positioned underneath the biomimetic leaf, and we image it by reflection thanks to a semi-reflective glass so the air-filled channels appear bright on the CMOS monochrome camera (PixeLink PL-B741U). As the PDMS is permeable to water and the leaf is exposed to a dry circulating air flow, the water in the channels pervaporates through the PDMS membrane. As soon as the device is out of water, it starts pervaporating and as the time needed to prepare the experiment is fluctuating, we define the reference time as the moment the first channel gets embolized. The air gradually invades the system from the cut at the petiole. The embolism spreads through the network, air replacing water. We capture a picture of the embolizing leaf every 10 s and make a time-lapse for the duration of the experiment which is about 5 h. The result is a stack of images to be treated. We also record simultaneously the deformation of a chosen channel ceiling, as described in the next subsection, in order to measure the pressure within the network.

2.2. Deformation measurement

2.2.1. State of the art

Several methods have been used to measure pressure or deformation in microfluidics systems. In [31], the authors use a fluorescence technique to probe channel deformation during pressure-driven flows. In [32], the authors use multiplexed PDMS integrated pressure sensors using the refraction effect of the pressure-induced curvature of PDMS ceiling. Here, additional circular side channels need to be added to the main microfluidic circuit. In [33], the same kind of approach is used. In [34], the authors have also developed a pressure sensor based on the measurement of channel ceiling deformation, but this time with interferometry using monochromatic light and fringe counting. We have developed also an interferometric method, but different in its implementation. One originality of our approach lies in the fact that the measurement place can be chosen, it is directly on the fluidic channel used, and it does not require an additional side channel. As we describe below, another originality lies in the interferometric method that uses white light and a spectrometer, allowing a direct absolute measurement of thickness and not a fringe number-based measurement that is in fact a relative method that needs to have knowledge of the initial pressure.

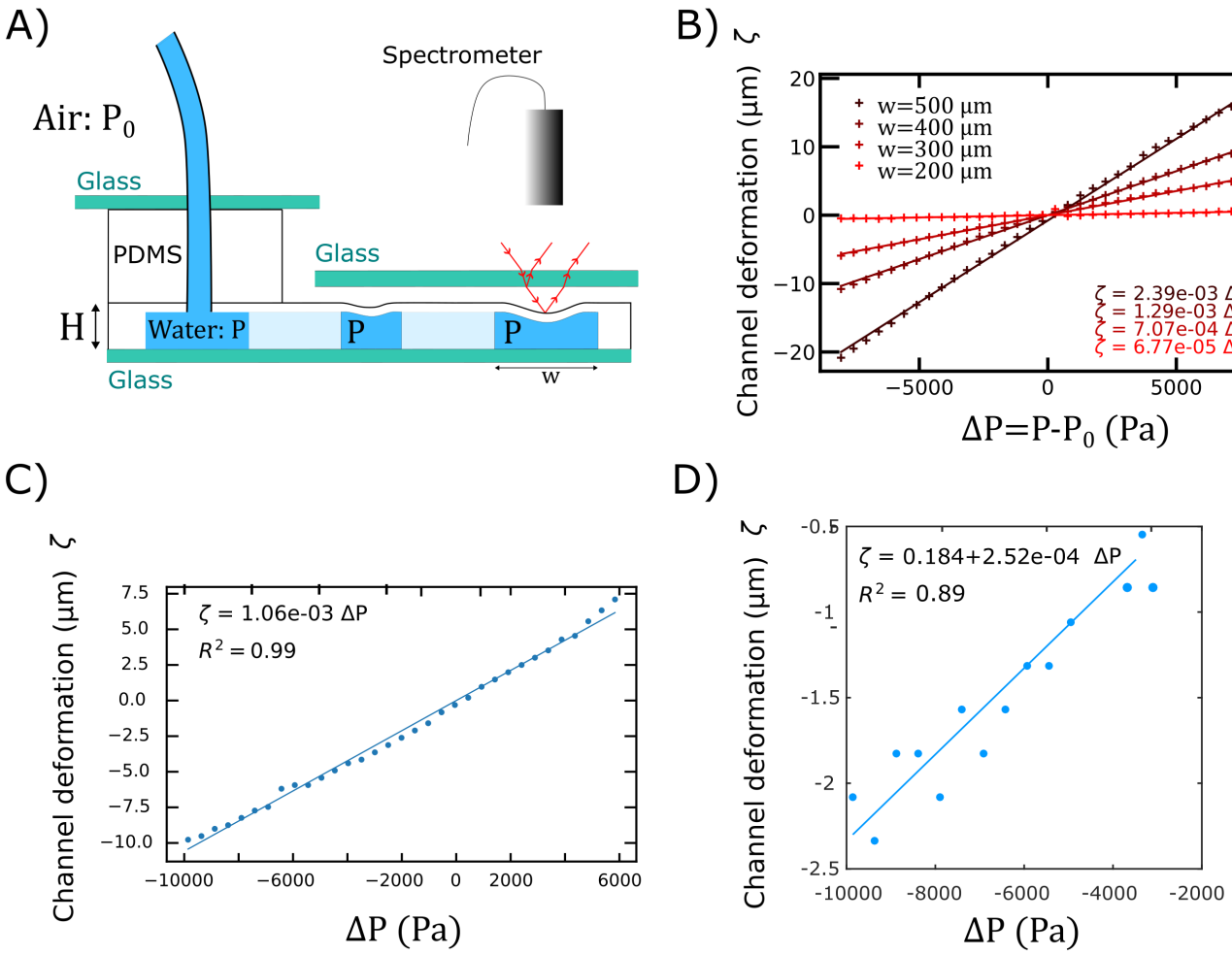

Figure 3. (A) Setup for the calibration of pressure ΔP versus ceiling deformation ζ curves. (B) Calibration curve on two-dimensional systems similar to the ones used in experiments, for which different channel widths have been tested. (C) Calibration curve obtained *a posteriori* on a channel after an experiment was done, in a two-dimensional system and in (D) for a one-dimensional system.

2.2.2. Experimental setup

The setup we developed to measure the pressure in the channel during the embolization of the device is schematized in figure 2. The pressure is calculated from the resulting deformations of the channel ceiling under the effect of the depression or repressurization in the channel during embolism. To measure the deflection of the ceiling, we used an interferometry-based method. However, as water and PDMS optical indices are too close to directly use interferometry, we created an extra air layer by adding a glass slide some tenths of micrometres over the system (figure 2). Dry air is circulated in this space to ensure that the device dries. We obtain the deflection of the membrane by measuring the thickness of this air layer over time.

Combined with a halogen light source (Ocean Optics HL-2000-FHSA) and an optical fibre, the spectrometer (Ocean Optics Flame-T) is positioned directly above a channel and supplies the wavelength spectrum to a program that computes the air thickness every two seconds by a Fourier transform which then gives the channel deformation ζ. Deformation at rest is measured when the channel is fully embolized, so the air inside is assumed to be at the pressure of the laboratory atmosphere.

2.2.3. Calibration

We performed calibration experiments for a channel element of a given width and a given ceiling thickness, to relate the deformation of the channel ceiling to the pressure in the channel element. More precisely, we impose the pressure (by gravity) in the channel and simultaneously measure the resulting deformation of the membrane with the spectrometer. We obtained a linear relation between the deformation of the membrane and the pressure in the channel element (figure 3). So, for a channel element of a given width and a given ceiling thickness, we can deduce the pressure in the channel by measuring the deformation of its ceiling. We made this calibration for the different channels of the biomimetic leaf (figure 3).

This calibration has been done following two methods: (i) on similar devices to the one used in the experiments, for which the inlet for pressurized water was bonded by plasma (but then not used in evaporation experiments); (ii) on the exact same devices that were used for experiments, with a scar at the inlet over which a PDMS piece was pressed on. This *a posteriori* calibration allows us to obtain it over the same exact device used for experiments. A perforated PDMS block is placed at the level of the cut in the petiole and maintained with clamps to ensure impermeability. The device is then filled with water and connected to a syringe via a tube. We then vary the altitude of the syringe and can compute the channel deformation for different pressures.

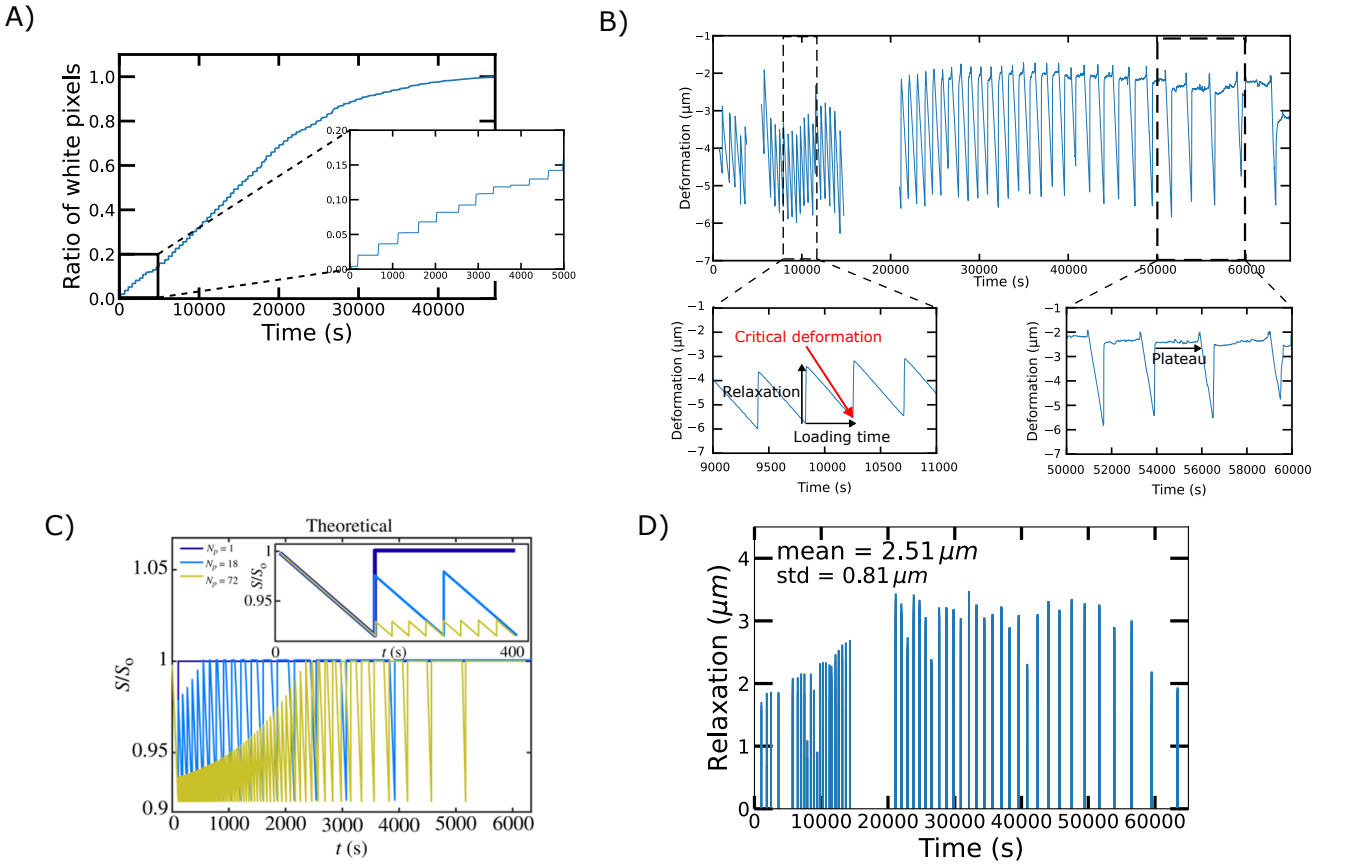

Figure 4. (A) Ratio of detected white pixels in a one-dimensional system versus time. This graph corresponds to the embolized percentage versus t, as represented by Brodribb *et al.* [13]. (B) Deformation ζ as a function of time for the same one-dimensional system. (C) Theoretical curves predicted by Keiser *et al.* [15] for the section area of the channel S rescaled by the nominal section area $S_0 = h_0 w$. The colours correspond to a number of constrictions $N_p = 1$, $N_p = 18$ and $N_p = 72$ for, respectively, the purple, the blue and the yellow curves. A value of S/S_0 smaller than 1 corresponds to a negative deformation ζ, or a depression inside the liquid-filled channels. (D) Relaxation, or jump amplitude of the deformation as a function of time.

3. Results

3.1. One-dimensional system

In figure 4A, we plot the ratio of embolized (white) pixels over time, which expresses the embolized fraction of the one-dimensional network [13]. Globally, the embolism rate slightly slows down over time (figure 4), because the evaporation flux is proportional to the wetted surface of the system [22,29,35]. By zooming, we observe an intermittent dynamics, sequences of arrests and jumps of the bubble, similar to the experiment of Keiser *et al.* [15].

From the deformation measurement setup, we estimate the channel maximal deformation ζ at its centre and plot it over time. The curve in figure 4B presents the deformation curve of the last channel element of the system, at the dead end. By zooming (two insets below), the graph for early time ($t < 20\,000$ s) shows an alternating gradual declines (during pervaporation and total volume decrease of water in all the system) and sharp increase when the meniscus unpins. This means a succession of depressurization and sudden relaxation of the measured channel. This phenomenon repeats itself whenever the embolism passes a constriction. The cycle frequency decreases during the experiment whereas the amplitude of the jumps of deformation ζ increases with time. During this first part of the experiment, the jumps of the embolism are complete (and the pressure relaxation is incomplete) and correspond to going directly from the situation depicted at t_2 in figure 1C to that depicted at t_4. Namely, the interface suddenly jumps from one constriction to the other pinning constriction where its propagation is momentarily arrested. For the second part of the experiment ($t > 20\,000$ s), as seen on the second inset (right graph), the amplitude of the jumps is more or less constant and the frequency is still decreasing. Instead of presenting a slow decrease and sharp increase, it passes then by a plateau phase since when the meniscus jumps, it does not fully advances in the channel element. As drawn in figure 1C, this corresponds to the situation at time t_3. During all the moments where the meniscus displaces inside a channel element, the deformation stays constant. The jumps are incomplete, but the pressure relaxations are complete.

Concerning the distribution of the waiting times Δt, a detailed discussion is provided in [15]. Here, we are in a situation that corresponds to a large number of channel elements N_p and which is similar as predicted theoretically in [15]. In figure 4C, the theoretical predictions from the model of [15] concerning the relative surface area variation of the section of the channel, S/S_0, is plotted for different values of N_p. In particular, the large N_p case (yellow curve) exhibits strong similarities with our measurements present in figure 4B. Indeed, in the small deformations regime, the section S and the deformation ζ are linked by an affine relation

as: $S = h.w$; $h(t) = h_0 + \zeta(t)$; $S = S_0 + 0.5\zeta * w$ and $S/S_0 = 1 + 0.5\zeta/h_0$. Note that ζ is taken negative as the channel is in depression ($\Delta P < 0$)

In figure 4D, we represent the amplitude of each jumps, also called relaxation (fast relaxation in pressure as noted in the inset). This allows an easy comparison with the curve from the theoretical approach from [15] in figure 4C. We observe the same trends as discussed before on the increase in jumps amplitude, reaching a plateau. The data are notably noisy, even in this device in one dimension with all constrictions and channels being identical.

3.1.1. Comparison between theoretical and experimental amplitude of pressures jumps

The average value for the jumps is around 2.5 µm and the plateau value is close to 3 µm. Using the calibration made for the one-dimensional system, we can determine the corresponding pressure differences.

The theoretical pressure differences at which the meniscus passes through a constriction are given by the Laplace law and for a rectangular section being $h_c = 48$ µm and $w_c = 22$ µm, it is written as $\Delta P_c = \gamma\kappa$, with :

$$\kappa = \frac{\left(1 + \frac{w_c}{h_c}\right) + \sqrt{\left(1 - \frac{w_c}{h_c}\right)^2 + \pi\left(\frac{w_c}{h_c}\right)}}{w_c}, \tag{3.1}$$

the maximal curvature of the interface in the constriction, and $\gamma = 72$ mN m^{-1} the surface tension of pure water. Here, the threshold given by the Laplace pressure is then equal to: $\Delta P_c(\text{theo}) = 9079$ Pa, assuming no effect of contact angle.

We can compare this value to the measurements deduced from the plateau value of the deformation ζ in figure 4D, which is about 3 µm. In terms of pressure, using the calibration carried out in figure 3D, this corresponds to $\Delta P_c(\text{exp}) = 11\,905$ Pa. This experimental value of the pressure jump is then slightly higher, but in quite good agreement with the theoretical value $P_c(\text{theo}) = 9079$ Pa. The relative error in relation to the experimental value is 24%. This discrepancy is likely to be due to several reasons. (i) The experiment shows a continuous distribution of pressure jumps, but the value kept is just a characteristic value of the highest jumps. (ii) Experimental errors on the calibration curve (which produce absolute differences, but give high relative precision). (iii) The actual three-dimensional shape and dimensions of the constrictions. In particular, the corners of the microfluidic channels are not perfectly fabricated as desired when drawn. Any dust or roughness leading to a local decrease of the value of w and h, even localized, will lead to an underestimation of the 'theoretical' value for the pressure jump. This will be explored in future studies and is linked in real plants to the higher complexity than expected by a simple formula giving the Laplace law pressure difference.

The maximal possible curvature compatible with the geometrical constraints only depends on the size of the constriction (the most important is the width when smaller than the thickness, but this latter is also important). The thinner the constriction, the greater the pressure difference required for the meniscus to pass through it.

The length of a meniscus jump depends directly on the amount of water lost by the system during the loading time. At the beginning of the experiment with still a big water reservoir, a great amount of water pervaporates during the loading time. By mass conservation, the potential length of the meniscus jump is proportional to this volume. Depending on the size of the exit channel, this jump can be limited and the new front directly pinned to the next constrictions. In that case, the depression in the liquid volume is not completely released, and a new loading starts directly after the jump. If the exit channel volume is large enough compared to the potential length of the meniscus jump, then meniscus stops inside the exit channel.

3.1.2. Comparison between hydrodynamic and capillary pressures

Between two neighbouring channels, the constriction resistance is $R_h = 12\eta L_c/(1 - 0.63\frac{w_c}{h_c})h_c w_c^3$ for a rectangular channel and the flux is about $Q_{pv} \simeq q_{lin}\frac{w}{\delta}L$ with $q_{lin} = D_p C_p^{sat}(1 - RH)$ [14,29]. Taking for the constriction dimensions: $L_c = 230$µm for its length, $w_c = 22$µm for its width, and $h_c = 48.3$µm for its height, we can deduce the hydrodynamic resistance $R_h = 7.53 \times 10^{12}$ Pa s m^{-3} and thereby the pressure loss due to viscous dissipation: $\Delta P_{hydro} = R_h Q_{pv} \sim 3 \times 10^{-1}$Pa. On the other hand, the pressure difference imposed by capillarity is about $\Delta P_{cap} = \frac{\gamma}{w_c} \sim 7 \times 10^3$Pa.

One thus has $\Delta P_{\text{cap}} >> \Delta P_{\text{hydro}}$, which leads us to assume that the pressure is uniform in the liquid volume, and that any pressure variations at the interface are quasi-instantaneously (compared to the typical timescale of the experiment imposed by pervaporation) transferred throughout the network.

3.2. Two-dimensional system

In the two-dimensional case, during the drying, the embolism front is made of several menisci in channels or constrictions. Once they are all pinned at constrictions, water-filled channels still pervaporate, lowering the pressure and shrinking channels until locally the pressure reaches a low enough value. After that, one meniscus jumps into its exit channel, suddenly increasing the pressure and relaxing the channel cross-section. The leaf is made of a pattern of water or air-connected domains; hence, clusters form that can isolate water-connected domains. Each of these clusters is then independent from a hydrodynamic point of view. This can be seen for example in figure 5C for $t = 4012$ s.

The deformation curve is much less regular than in the one-dimensional case. We have used the calibration curve to plot here directly the pressure, as shown in figure 5B. The jumps are globally increasing in amplitude on average, as in the one-dimensional case, but they show a larger variability and randomness for their height and the waiting time between two relaxations.

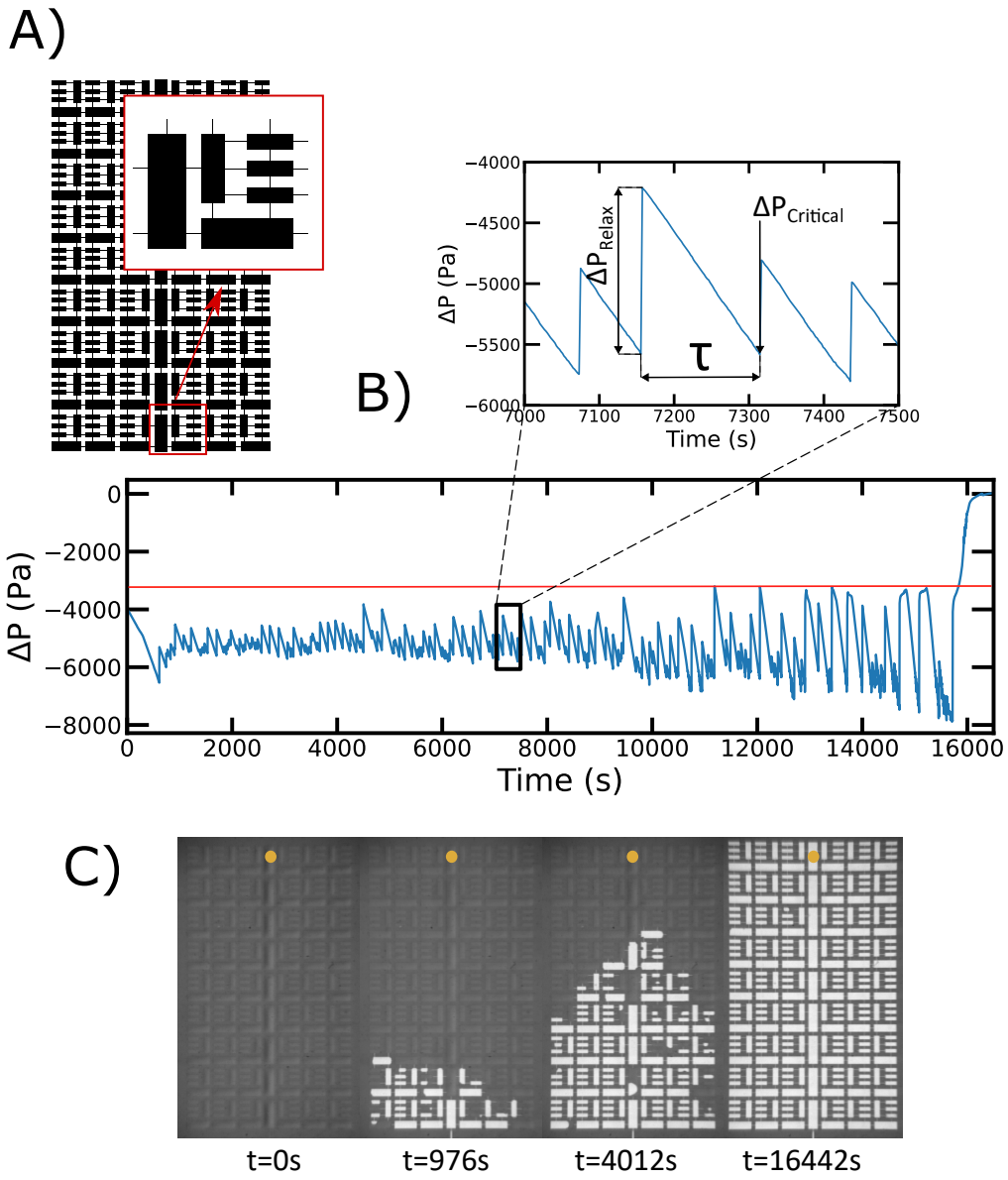

Figure 5. (A) Schematic of a two-dimensional device with various channel sizes. (B) Evolution with time of the ceiling deformation of the channel pointed in (C). (C) Embolism spreading with time. White domain represents the spreading air embolism. The yellow dot points the channel element where the deformation is measured over time. It corresponds to the largest channel element, at the end of the main vein, the most far away from petiole (start of the embolism).

Here, the width of the constriction is $w_c = 20\,\mu m$ and height $h_c = 38\,\mu m$. The theoretical critical pressure for the full jump is then, following equation (3.1), $\Delta P_c(\text{theo}) = 10\,426$ Pa. In the experiment, the critical pressure for each passed constriction is given by the lowest value of each slow pressure decrease curve $\Delta P_{\text{Critical}}$, as indicated by the inset in figure 5B. The values lie between 6000 and 8000 Pa, which is a bit lower than the expected theoretical critical pressure of $\Delta P_c(\text{theo}) = 10\,426$ Pa. It is normal that for not complete pressure relaxation, the jumps are lower.

4. Discussion

For one-dimensional systems, we find that the measured deformation curves agree closely with the theoretical predictions from [15], reproducing key features such as jump frequencies, jump amplitudes, waiting times Δt and both complete and incomplete relaxation. Two main slight discrepancies can be noted: (i) the critical pressure at which each jump occurs varies, largely due to microfabrication imperfections that make each constriction slightly different, and (ii) the calibration used to convert deformation into absolute pressure values could be refined, especially in stiff channels with thicker PDMS layers. Nonetheless, these results strongly support our hypothesis that pressure is effectively uniform in the liquid phase, given that hydrodynamic resistance remains much smaller than capillary forces in these geometries. Our two-dimensional systems, introduced here for the first time, exhibit significantly more complex behaviour with higher randomness in the timing and magnitude of pressure jumps, as well as the formation of spatial clusters of embolized channels. Even though the constrictions in our two-dimensional devices are nominally identical, the interconnected topology naturally promotes branching and multiple propagation pathways, in contrast to the simpler one-dimensional scenario. In future work, systematically varying constriction size and channel connectivity, or

introducing a hierarchy of vein-like orders, could reveal richer insights into how structural and topological factors drive intermittent embolism propagation. Likewise, although viscous losses are currently negligible, increasing the network size or narrowing the constrictions could make hydrodynamic pressure gradients more significant, altering the nature of the jumps and potentially mimicking a broader range of xylem conditions.

4.1. Perspectives

Having established an interferometry-based approach to measure *in situ* pressure variations, we believe that this artificial system can serve as a versatile platform for investigating embolism mechanics. However, several important biological features remain challenging to capture:

- *Pit membrane complexity*: In biological leaves, bordered pit membranes are highly multiscale porous structures—many orders of magnitude smaller than our micro-scale constrictions—and often composed of fibrous materials that selectively allow water passage while blocking air [19,26,36]. Our current channels do not replicate these nanoporous architectures, limiting the direct applicability of our results to natural pit function and in particular its ability to sustain pressures of several MPa.
- *Complex venation and apoplastic and symplastic pathways*: Leaf veins in many species consist of bundles of parallel conduits rather than a single channel [37–40]. This arrangement can produce overlapping embolism events and more complex front dynamics compared to the single-channel geometry used here. The two-dimensional network presented in this article is a first step towards the development of realistic xylem network topology. Furthermore, biological leaves exhibit parallel transport through living and nonliving tissues. By comparison, our artificial networks provide a simplified apoplastic path with no active symplastic transport. Future steps could consist of including osmotic effects in parallel, with phloem-like microchannels [41,42], as well as active microfluidic components to mimic cellular activity.
- *Material properties, negative pressures and hygroscopicity*: Our PDMS membranes, while convenient for fabrication, are not sufficiently stiff to sustain the large negative pressures encountered in xylem. Consequently, we operate at positive pressures that favour external air seeding over cavitation. Materials such as hydrogels or stiffer composites might enable negative pressures, facilitating studies on how cavitation events interact with air seeding and nanobubble formation [10,17,43]. Unlike real leaves, which have substantial water exchange between veins and surrounding tissues [44,45], our PDMS has low hygroscopicity. This restricts the potential for internal water storage and subsequent release, an important aspect of the hydraulic capacitance in living tissues [46,47]. Again, resorting to hydrogels could offer more realistic materials concerning the water exchange aspects.

By addressing these points, we aim to bridge the gap between purely 'bio-inspired' microfluidic channels and the genuine complexity of xylem in real leaves. Our current tool, combining a PDMS leaf analogue with a noninvasive interferometric pressure sensor, already offers rich insights into elastocapillary-driven air invasion. With further improvements in material selection, channel topology, and pore-scale structure, it may become a powerful, integrated platform for testing hypotheses about embolism formation and propagation in plant-like systems.

5. Conclusion

(1) We presented a new non-invasive interferometric technique to measure the instantaneous pressure variation during elastocapillary propagation of gaseous embolisms in biomimetic leaves.
(2) The measured pressure jumps over time closely match the capillary threshold predicted by Laplace's law, demonstrating that constriction geometry and interface curvature are key factors.
(3) Two-dimensional networks exhibit more complex and stochastic dynamics than their one-dimensional counterparts, underscoring the importance of network topology in embolism propagation.
(4) Further refinements in pressure measurement and more detailed modelling of real plant microstructures will be needed to address remaining discrepancies between experiments and theory, particularly in interpreting pressure jumps at the microscale.

Ethics. This work did not require ethical approval from a human subject or animal welfare committee.

Data accessibility. Data are available on Zenodo [48].

Declaration of AI use. We have not used AI-assisted technologies in creating this article.

Authors' contributions. F.-X.G.: data curation, investigation, methodology, writing—original draft, writing—review and editing; L.J.: conceptualization, formal analysis, methodology, writing—review and editing; L.K.: conceptualization, formal analysis, methodology, supervision, writing—original draft, writing—review and editing; C.C.: conceptualization, funding acquisition, methodology, project administration, supervision, writing—review and editing; X.N.: conceptualization, formal analysis, funding acquisition, methodology, project administration, supervision, writing—original draft, writing—review and editing.

All authors gave final approval for publication and agreed to be held accountable for the work performed therein.

Conflict of interest declaration. We declare we have no competing interests.

Funding. This work has been supported by French government, through the grant ANR-19-CE30-0010-02 (PHYSAP) and through the UCA^{JEDI} Investments in the Future project managed by the National Research Agency (ANR) with the reference number ANR-15-IDEX-01. We also acknowledge the Université Côte d'Azur (UniCA) for funding.

Acknowledgements. We thank Philippe Marmottant and Benjamin Dollet for fruitful discussions. We thank Virgile Thiévenaz for the walnut tree image. We thank JRSI for the image taken from [15] in figure 4.

References

1. Llorens C, Argentina M, Rojas N, Westbrook J, Dumais J, Noblin X. 2016 The fern cavitation catapult: mechanism and design principles. *J. R. Soc. Interface* **13**, 20150930. (doi:10.1098/rsif.2015.0930)
2. Scognamiglio C, Magaletti F, Izmaylov Y, Gallo M, Casciola CM, Noblin X. 2018 The detailed acoustic signature of a micro-confined cavitation bubble. *Soft Matter* **14**, 7987–7995. (doi:10.1039/c8sm00837j)
3. Dixon H, Joly J. 1895 XII. On the ascent of sap. *Phil. Trans. R. Soc. Lond. B* **186**, 563. (doi:10.1098/rstb.1895.0012)
4. Tyree MT, Zimmermann MH. 2013 *Xylem structure and the ascent of sap*. Berlin, Germany: Springer Science & Business Media.
5. Stroock AD, Pagay VV, Zwieniecki MA, Michele Holbrook N. 2014 The physicochemical hydrodynamics of vascular plants. *Annu. Rev. Fluid Mech.* **46**, 615–642. (doi:10.1146/annurev-fluid-010313-141411)
6. Venturas MD, Sperry JS, Hacke UG. 2017 Plant xylem hydraulics: what we understand, current research, and future challenges. *J. Integr. Plant Biol.* **59**, 356. (doi:10.1111/jipb.12534)
7. Choat B, Badel E, Burlett R, Delzon S, Cochard H, Jansen S. 2016 Noninvasive measurement of vulnerability to drought-induced embolism by X-Ray microtomography. *Plant Physiol.* **170**, 273–282. (doi:10.1104/pp.15.00732)
8. Wagner Y, Feng F, Yakir D, Klein T, Hochberg U. 2022 In situ, direct observation of seasonal embolism dynamics in Aleppo pine trees growing on the dry edge of their distribution. *New Phytol.* **235**, 1344–1350. (doi:10.1111/nph.18208)
9. Choat B, Brodribb TJ, Brodersen CR, Duursma RA, López R, Medlyn BE. 2018 Triggers of tree mortality under drought. *Nature* **558**, 531–539. (doi:10.1038/s41586-018-0240-x)
10. Kanduč M, Schneck E, Loche P, Jansen S, Schenk HJ, Netz RR. 2020 Cavitation in lipid bilayers poses strict negative pressure stability limit in biological liquids. *Proc. Natl Acad. Sci. USA* **117**, 10733–10739. (doi:10.1073/pnas.1917195117)
11. Cochard H. 2006 Cavitation in trees. *Comput Rendus Phys.* **7**, 1018–1026. (doi:10.1016/j.crhy.2006.10.012)
12. Schenk HJ *et al*. 2017 Xylem surfactants introduce a new element to the cohesion-tension theory. *Plant Physiol.* **173**, 1177–1196. (doi:10.1104/pp.16.01039)
13. Brodribb TJ, Bienaimé D, Marmottant P. 2016 Revealing catastrophic failure of leaf networks under stress. *Proc. Natl Acad. Sci. USA* **113**, 4865–4869. (doi:10.1073/pnas.1522569113)
14. Keiser L, Marmottant P, Dollet B. 2022 Intermittent air invasion in pervaporating compliant microchannels. *J. Fluid Mech.* **948**, A52. (doi:10.1017/jfm.2022.733)
15. Keiser L, Dollet B, Marmottant P. 2024 Embolism propagation in *Adiantum* leaves and in a biomimetic system with constrictions. *J. R. Soc. Interface* **21**, 20240103. (doi:10.1098/rsif.2024.0103)
16. Brodribb TJ, Skelton RP, McAdam SAM, Bienaimé D, Lucani CJ, Marmottant P. 2016 Revealing catastrophic failure of leaf networks under stress. *New Phytol.* **209**, 1403. (doi:10.1111/nph.13846)
17. Schenk HJ, Steppe K, Jansen S. 2015 Nanobubbles: a new paradigm for air-seeding in xylem. *Trends Plant Sci.* **20**, 199–205. (doi:10.1016/j.tplants.2015.01.008)
18. Silva LM, Pfaff J, Pereira L, Miranda MT, Jansen S. 2024 Embolism propagation does not rely on pressure only: time-based shifts in xylem vulnerability curves of angiosperms determine the accuracy of the flow-centrifuge method. *Tree Physiol.* tpae131. (doi:10.1093/treephys/tpae131)
19. Zhang Y, Pereira L, Kaack L, Liu J, Jansen S. 2024 Gold perfusion experiments support the multi-layered, mesoporous nature of intervessel pit membranes in angiosperm xylem. *New Phytol.* **242**, 493–506. (doi:10.1111/nph.19608)
20. Li S, Lens F, Espino S, Karimi Z, Klepsch M, Schenk HJ, Schmitt M, Schuldt B, Jansen S. 2016 Intervessel pit membrane thickness as a key determinant of embolism resistance in angiosperm xylem. *IAWA J.* **37**, 152–171. (doi:10.1163/22941932-20160128)
21. Jensen KH, Berg-Sørensen K, Bruus H, Holbrook NM, Liesche J, Schulz A, Zwieniecki MA, Bohr T. 2016 Sap flow and sugar transport in plants. *Rev. Mod. Phys.* **88**, 035007. (doi:10.1103/RevModPhys.88.035007)
22. Noblin X, Mahadevan L, Coomaraswamy IA, Weitz DA, Holbrook NM, Zwieniecki MA. 2008 Optimal vein density in artificial and real leaves. *Proc. Natl Acad. Sci. USA* **105**, 9140–9144. (doi:10.1073/pnas.0709194105)
23. Berg S *et al*. 2013 Real-time 3D imaging of Haines jumps in porous media flow. *Proc. Natl Acad. Sci. USA* **110**, 3755–3759. (doi:10.1073/pnas.1221373110)
24. Vergeynst LL, Sause MGR, De Baerdemaeker NJF, De Roo L, Steppe K. 2016 Clustering reveals cavitation-related acoustic emission signals from dehydrating branches. *Tree Physiol.* **36**, 786–796. (doi:10.1093/treephys/tpw023)
25. De Baerdemaeker NJF, Stock M, Van den Bulcke J, De Baets B, Van Hoorebeke L, Steppe K. 2019 X-ray microtomography and linear discriminant analysis enable detection of embolism-related acoustic emissions. *Plant Methods* **15**, 153. (doi:10.1186/s13007-019-0543-4)
26. Kaack L *et al*. 2021 Pore constrictions in intervessel pit membranes provide a mechanistic explanation for xylem embolism resistance in angiosperms. *New Phytol.* **230**, 1829–1843. (doi:10.1111/nph.17282)
27. Scoffoni C, Albuquerque C, Brodersen CR, Townes SV, John GP, Cochard H, Buckley TN, McElrone AJ, Sack L. 2017 Leaf vein xylem conduit diameter influences susceptibility to embolism and hydraulic decline. *New Phytol.* **213**, 1076–1092. (doi:10.1111/nph.14256)
28. Scoffoni C, Albuquerque C, Brodersen CR, Townes SV, John GP, Bartlett MK, Buckley TN, McElrone AJ, Sack L. 2017 Outside-xylem vulnerability, not xylem embolism, controls leaf hydraulic decline during dehydration. *Plant Physiol.* **173**, 1197–1210. (doi:10.1104/pp.16.01643)
29. Dollet B, Louf JF, Alonzo M, Jensen KH, Marmottant P. 2019 Drying of channels by evaporation through a permeable medium. *J. R. Soc. Interface* **16**, 20180690. (doi:10.1098/rsif.2018.0690)
30. McDonald JC, Duffy DC, Anderson JR, Chiu DT, Wu H, Schueller OJ, Whitesides GM. 2000 Fabrication of microfluidic systems in poly(dimethylsiloxane). *Electrophoresis* **21**, 27. (doi:10.1002/(SICI)1522-2683(20000101)21:1<27::AID-ELPS27>3.0.CO;2-C)
31. Hardy BS, Uechi K, Zhen J, Kavehpour HP. 2009 The deformation of flexible PDMS microchannels under a pressure driven flow. *Lab Chip* **9**, 935. (doi:10.1039/B813061B)
32. Orth A, Schonbrun E, Crozier KB. 2011 Multiplexed pressure sensing with elastomer membranes. *Lab Chip* **11**, 3810–3815. (doi:10.1039/c1lc20114j)
33. Raventhiran N, Molla RS, Nandishwara K, Johnson E, Li Y. 2022 Design and fabrication of a novel on-chip pressure sensor for microchannels. *Lab Chip* **22**, 4306–4316. (doi:10.1039/d2lc00648k)
34. Song W, Psaltis D. 2011 Optofluidic membrane interferometer: an imaging method for measuring microfluidic pressure and flow rate simultaneously on a chip. *Biomicrofluidics* **5**, 44110–4411011. (doi:10.1063/1.3664693)
35. Bacchin P, Leng J, Salmon JB. 2022 Microfluidic evaporation, pervaporation, and osmosis: from passive pumping to solute concentration. *Chem. Rev.* **122**, 6938–6985. (doi:10.1021/acs.chemrev.1c00459)
36. Zhang Y *et al*. 2020 High porosity with tiny pore constrictions and unbending pathways characterize the 3D structure of intervessel pit membranes in angiosperm xylem. *Plant Cell Environ.* **43**, 116–130. (doi:10.1111/pce.13654)

37. Loepfe L, Martinez-Vilalta J, Piñol J, Mencuccini M. 2007 The relevance of xylem network structure for plant hydraulic efficiency and safety. *J. Theor. Biol.* **247**, 788–803. (doi:10.1016/j.jtbi.2007.03.036)
38. Roth-Nebelsick A. 2019 It's contagious: calculation and analysis of xylem vulnerability to embolism by a mechanistic approach based on epidemic modeling. *Trees* **33**, 1519–1533. (doi:10.1007/s00468-019-01891-w)
39. Mrad A, Johnson DM, Love DM, Domec JC. 2021 The roles of conduit redundancy and connectivity in xylem hydraulic functions. *New Phytol.* **231**, 996–1007. (doi:10.1111/nph.17429)
40. Roth-Nebelsick A, Konrad W. 2023 *Xylem: methods and protocols*, pp. 17–34. New York, NY: Humana. (doi:10.1007/978-1-0716-3477-6_2)
41. Jensen KH, Rio E, Hansen R, Clanet C, Bohr T. 2009 Osmotically driven pipe flows and their relation to sugar transport in plants. *J. Fluid Mech.* **636**, 371–396. (doi:10.1017/S002211200900799X)
42. Comtet J, Jensen KH, Turgeon R, Stroock AD, Hosoi AE. 2017 Passive phloem loading and long-distance transport in a synthetic tree-on-a-chip. *Nat. Plants* **3**, 17032. (doi:10.1038/nplants.2017.32)
43. Ingram S, Jansen S, Schenk HJ. 2023 Lipid-coated nanobubbles in plants. *Nanomaterials* **13**, 1776. (doi:10.3390/nano13111776)
44. Sack L, Holbrook NM. 2006 Leaf hydraulics. *Annu. Rev. Plant Biol.* **57**, 361–381. (doi:10.1146/annurev.arplant.56.032604.144141)
45. Blackman CJ, Brodribb TJ. 2011 Two measures of leaf capacitance: insights into the water transport pathway and hydraulic conductance in leaves. *Funct. Plant Biol.* **38**, 118–126. (doi:10.1071/FP10183)
46. Hölttä T, Cochard H, Nikinmaa E, Mencuccini M. 2009 Capacitive effect of cavitation in xylem conduits: results from a dynamic model. *Plant Cell Environ.* **32**, 10–21. (doi:10.1111/j.1365-3040.2008.01894.x)
47. Meinzer FC, Johnson DM, Lachenbruch B, McCulloh KA, Woodruff DR. 2009 Xylem hydraulic safety margins in woody plants: coordination of stomatal control of xylem tension with hydraulic capacitance. *Funct. Ecol.* **23**, 922–930. (doi:10.1111/j.1365-2435.2009.01577.x)
48. Noblin X, Gauci FX, Keiser L, Cohen C, Jami L. 2025 Channel deformations during elastocapillary spreading of gaseous embolisms in biomimetic leaves [Data set]. Zenodo. (doi:10.5281/zenodo.15061894)